

Modeling Athermal Phonons in Novel Materials using the G4CMP Simulation Toolkit

I. Hernandez^{a,b}, R. Linehan^{†b}, R. Khatiwada^{a,b}, E. Figueroa-Feliciano^{d,b}, L. Hsu^b, M. Kelsey^c

^a*Illinois Institute of Technology, Department of Physics, Chicago, IL 60616, USA*

^b*Fermi National Accelerator Laboratory Laboratory, Batavia, IL 60510, USA*

^c*Texas A&M University, 400 Bizzell St. College Station, TX 77843*

^d*Department of Physics & Astronomy, Northwestern University, Evanston, IL 60208, USA*

Abstract

Understanding phonon and charge propagation in superconducting devices plays an important role in both performing low-threshold dark matter searches and limiting correlated errors in superconducting qubits. The Geant4 Condensed Matter Physics (G4CMP) package, originally developed for the Cryogenic Dark Matter Search (CDMS) experiment, models charge and phonon transport within silicon and germanium detectors and has been validated by experimental measurements of phonon caustics, mean charge-carrier drift velocities, and heat pulse propagation times. In this work, we present a concise framework for expanding the capabilities for phonon transport to a number of other novel substrate materials of interest to the dark matter and quantum computing communities, including sapphire (Al_2O_3), Gallium Arsenide (GaAs), Lithium Fluoride (LiF), Calcium Tungstate (CaWO_4), and Calcium Fluoride (CaF_2). We demonstrate the use of this toolkit in generating phonon transport properties of these materials and compare these properties with experimentally-determined values where available.

Keywords: Phonon, Simulation, G4CMP, Dark Matter, Material Science, Qubits, Sapphire

1 1

2 1 Introduction

3 Mounting astrophysical and cosmological ob-
4 servations indicate the existence and abundance of
5 a cold, frictionless nonbaryonic “dark” matter in
6 the universe [1, 2, 3]. As direct detection searches
7 for particle-like candidates with masses above the
8 GeV/c^2 scale have yielded only null results in the
9 past few decades [4, 5], there has recently been in-
10 creased interest in developing low-energy threshold
11 detectors capable of probing parameter space at
12 lower masses down to the keV/c^2 scale [6]. A com-
13 mon class of such detectors rely on cryogenic (mK)
14 solid-state substrates coupled to superconducting
15 films, in which energy depositions in the substrate
16 generate phonon excitations that can be sensed in
17 the films [7, 8, 9, 10]. These phonons may be gen-
18 erated from a number of different potential inter-
19 action types: direct nuclear recoils of dark matter
20 on lattice ions, phonons produced from electron-
21 hole recombination after a dark matter ionization
22 event, and Neganov-Trofimov Luke phonons from
23 drifting freed electrons through the crystal using

an electrostatic field. The phonon response of sil-
icon and germanium under these effects has been
well-studied [11, 12, 13, 14]

In recent years there has been a broadening
of the landscape of materials proposed for
phonon-mediated cryogenic dark matter search
experiments. While historically these detectors
have been made from silicon, germanium, cal-
cium tungstate (CaWO_4), or calcium fluoride
(CaF_2) [15, 16, 17, 18], future dark matter de-
tectors may benefit from other carefully chosen
novel target materials. For example, polar crys-
tals like sapphire (Al_2O_3) and gallium arsenide
(GaAs) increase sensitivity to DM candidates cou-
pling to the dark photon. These materials, espe-
cially those with many accessible optical modes,
give sufficiently strong directional dependence of
DM scattering rates to enable daily modulation
searches, increasing DM discovery power [19, 20].
A thorough grasp of (and ability to model) phonon
propagation in these materials will be required for
signal- and background-model building in these ex-
periments.

Moreover, some of these materials (like saphire)
are commonly used in the quantum comput-
ing community as chip substrates due to their low
dielectric losses [21]. As superconducting qubits
have been shown to experience catastrophic corre-
lated errors due to the presence of phonons pro-

[†]linehan3@fnal.gov

53 duced by ionizing radiation, developing a quantitative
54 understanding of phonon transport in such chips may facilitate developing strategies that mitigate
55 such errors [22, 23, 24, 25].

56 Modeling phonon propagation in novel materials is therefore a foundation for studying signals and backgrounds in particle-like dark matter searches and sources of correlated errors in superconducting qubits. The Geant4 Condensed Matter Physics (G4CMP) package is an open-source particle-tracking simulation tool built to perform this modeling, originally in the context of low-mass dark matter experiments [26]. While it successfully models phonon transport within silicon and germanium substrates, it currently does not include information for phonon propagation in other target materials. As other substrate materials are adopted in dark matter searches or quantum computing, a thorough understanding of chip response to energy depositions will rely on a corresponding expansion of the set of materials in which G4CMP can model phonon transport.

57 In this work we achieve an expansion of G4CMP’s phonon-modeling capability for a large number of materials of interest to the low-mass dark matter and quantum information communities, and provide a framework for extending this to further materials. In Section 2, we discuss the phonon physics that underlies G4CMP’s transport modeling and present the set of parameters needed for modeling phonon response in a new material. In Section 3, we calculate this set of parameters for several new materials, demonstrate successful integration into G4CMP, and validate the results against experimental results available in the literature. We discuss potential extensions to this modeling and its impact on dark matter detection and quantum computing efforts in Section 4, and conclude in Section 5.

92 2 Phonon Kinematics

93 When high-energy phonons are created from energy deposits in a chip, the system evolves in a way governed by several distinct phonon kinematics processes. We consider as an example an optical phonon created from a DM scatter in the substrate. First, this phonon can undergo anharmonic decay into multiple lower-energy phonons via one of several possible channels, including the Klemens channel² ($\text{LO} \rightarrow \text{XA} + \text{XA}$), the Ri-

dley Channel ($\text{LO} \rightarrow \text{TO} + \text{XA}$), and the Valée-Bogani channel ($\text{LO} \rightarrow \text{LO} + \text{XA}$) [27]. All of these optical phonon decay channels occur on $\mathcal{O}(ps)$ timescales. Once downconversion from the optical branch phonons to acoustic branch phonons occurs, there is further downconversion of the acoustic phonons, fragmenting the initial phonon energy even more. Scattering on isotopic impurities may change acoustic phonon’s trajectories and polarizations, and has been noted to possibly also play a role in phonon thermalization [28]. Selection of the proper final-state phonon polarizations during downconversion and scattering is governed by the fractional density of states (DOS) for the various possible phonon polarizations. At sufficiently low acoustic phonon energies, the scattering and downconversion mean free paths may extend beyond the substrate dimensions, and the phonon trajectory becomes limited by boundary scatters (i.e. enters the “ballistic regime”). At all energies, phonon propagation is governed by the substrate’s crystal structure, leading to formation of caustics, preferred directions into which phonons’ group velocities are focused by the crystal anisotropy. G4CMP simulates the subset of these physical processes involving acoustic phonons: acoustic phonon anharmonic downconversion, isotopic scattering, and transport along caustics.³

94 The set of parameters needed to integrate this physics into G4CMP for a given material is enumerated in Table 1. Because rigorous modeling of some of the above-mentioned physics processes in a fully anisotropic medium is nontrivial, it is often useful to simplify calculations using the “isotropic continuum approximation,” (ICA) in which phonons are assumed to be long enough in wavelength that anisotropy in the crystal may be ignored [29]. While we (and G4CMP) use this approximation to simplify calculations of the rate coefficients for anharmonic decay and isotopic scattering, the DOS and caustics modeling fully accounts for the anisotropic crystal structure.

95 The thrust of this section is to discuss the mathematical foundation for these physics processes and estimate the corresponding required simulation parameters for a set of substrates useful to the dark matter detection community. In doing so we also hope to provide a streamlined recipe for performing this G4CMP upgrade for any other materials later deemed of interest to the cryogenic instrumentation community.

96 ²Here, LO indicates longitudinal optical phonon modes,
97 TO indicates transverse optical modes, and XA indicates either longitudinal or transverse acoustic modes. In the acoustic mode, we keep this general as arbitrary combinations
98 may be energetically prohibited in certain materials depending on the phonon dispersion.

99 ³While scattering and downconversion of phonons at surfaces is simulated in G4CMP, the complexity of that topic puts it beyond the scope of this work. Optical phonons are not simulated in G4CMP.

Table 1: Parameters required for G4CMP to model phonon transport within a given solid-state material.

| Parameter | Units | Description |
|--------------|----------------|---|
| C_{ij} | GPa | Second-order elastic constants |
| μ | GPa | Lamé constant, 2nd-order isotropic elastic constant |
| λ | GPa | Lamé constant, 2nd-order isotropic elastic constant |
| β | GPa | 3rd-order isotropic elastic constant |
| γ | GPa | 3rd-order isotropic elastic constant |
| A | s ⁴ | Anharmonic downconversion rate coefficient |
| B | s ³ | Isotropic scattering rate coefficient |
| F_{TT} | None | Fraction of $L \rightarrow TT$ downconversion |
| LDOS | None | Longitudinal phonons' density of states (fractional) |
| STDOS | None | Slow transverse phonons' density of states (fractional) |
| FTDOS | None | Fast transverse phonons' density of states (fractional) |
| Debye Energy | THz | Debye Energy for phonon primaries |

2.1 Anharmonic Downconversion

Anharmonic decay of an acoustic phonon into two lower-energy acoustic phonons is phonon-polarization-dependent. Under the isotropic continuum approximation, this decay can only proceed for initial longitudinally-polarized phonons, and can only proceed via two potential decay channels: $L \rightarrow L + T$ and $L \rightarrow T + T$, in which the final products are a longitudinal (L) and transverse (T) phonon and two transverse phonons, respectively. Here, transverse phonons can be either on the transverse-slow phonon branch or transverse-fast phonon branch. Though beyond the scope of this work's modeling, we also note for completeness that additional decay modes, including those for transverse phonons, are possible if the ICA is relaxed [30, 31, 32].

Formally, the combined $L \rightarrow T + T$ and $L \rightarrow L + T$ rate of anharmonic decay within a crystal can be calculated by adding the third-order terms of the crystal's potential energy to the Hamiltonian governing the crystal's evolution. Using first-order time-dependent perturbation theory, one can derive a characteristic mode decay rate, $\Gamma_{\text{anharmonic}}$, with the following form:

$$\Gamma_{\text{anharmonic}} = A\nu^5, \quad (1)$$

where A is a temperature-independent constant [29, 33] and ν is the phonon frequency. This form holds for normal (i.e. non-Umklapp) phonon processes at low temperatures ($k_B T \ll h\nu$).

Calculating the constant A in Equation 1 relies on knowing the second- and third-order elastic constants considered in the total potential energy of the material. Here, it is useful to apply the ICA, giving rise to a separate set of “isotropic elastic constants:” the Lamé constants μ and λ at second order, and a set of three constants α , β , and γ at third order. Ref. [33] gives the $L \rightarrow T + T$ and

$L \rightarrow L + T$ decay rates in terms of these parameters.

To numerically calculate the decay rate in a material of a specific crystal structure, the isotropic elastic constants μ , λ , α , β , and γ can be expressed using the *true* second-order elastic constants C_{ijkl} and third-order elastic constants C_{ijklmn} corresponding to the material's crystal group. A general form of this parameterization is found using the development by Ref. [34], where Einstein notation is used:

$$\begin{aligned} \mu &= (3C_{lkkk} - C_{llkk})/30 \\ \lambda &= (2C_{lkkk} - C_{llkk})/15 \\ \alpha &= (8C_{iillnn} - 15C_{iilnln} + 8C_{inilln})/105 \quad (2) \\ \beta &= (-5C_{iillnn} + 19C_{iilnln} - 12C_{inilln})/210 \\ \gamma &= (2C_{iillnn} - 9C_{iilnln} + 9C_{inilln})/210. \end{aligned}$$

For a specific crystal space group these parameters can be calculated by taking advantage of symmetries present in the second- and third-order elastic constants [35]. Most of the materials of interest to the dark matter search community that we consider here, including Si, Ge, GaAs, LiF and CaF₂, belong to cubic space groups. For these, space-group-specific expressions for the second- and third-order isotropic elastic constants have been documented extensively in literature, and as a result we do not reproduce them here [34, 33, 36]. However, a few materials of interest, including sapphire (Al₂O₃) and calcium tungstate (CaWO₄), have non-cubic space groups for which expressions of α , β , γ , μ , and λ have not yet been documented in literature (to the authors' knowledge). In Table 2, we present expressions for these in terms of the materials' third-order elastic constants, using Voigt notation [37] for reduction from $2n$ to n in-

220 dices, where n is the order of the elastic constant.

221 Once these isotropic second- and third-order
222 elastic constants are calculated for a material,
223 the value A in Equation 1 can be calculated via
224 the treatment in Ref. [33], and used as an input
225 to G4CMP. Results of our calculations for vari-
226 ous materials of interest will be presented in Sec-
227 tion 3.1.

228 **2.2 Isotopic Scattering**

229 Phonons may also be scattered on isotopic
230 impurities in the crystal, where slight variations
231 in atomic mass break the regularity in the crys-
232 tal structure. Considering these impurities as a
233 small perturbation to the otherwise uniform crys-
234 tal Hamiltonian, one can again use perturbation
235 theory to obtain an expression for the scattering
236 rate of a single phonon via this channel [29]. This
237 rate is proportional to the fourth power of phonon
238 energy:

$$\Gamma_{\text{isotopic}} = B\nu^4 \quad (3)$$

$$= \frac{4\pi^3\Gamma_{md}\Omega}{\langle c^3 \rangle} \nu^4, \quad (4)$$

239 where Ω is the volume per atom in the crystal
240 unit cell, $\langle c^3 \rangle$ is the polarization-averaged (cubed)
241 speed of sound in the material, and Γ_{md} is a mass
242 defect coefficient capturing the average deviation
243 of the crystal from isotopic purity [38, 39]. This
244 expression holds true in the isotropic continuum
245 approximation, which holds for phonons with long
246 wavelengths relative to the interatomic spacing.
247 The mass defect coefficient is given by [40, 41]

$$\Gamma_{md} = \frac{\langle \overline{\Delta M^2} \rangle}{\langle \overline{M} \rangle^2}, \quad (5)$$

248 where $\langle \overline{\Delta M^2} \rangle$ refers to the average mass variance
249 and $\langle \overline{M} \rangle^2$ is the average mass. The average mass
250 of each component is given by the stoichiometry-
251 weighted average of each site average \overline{M}_n

$$\langle \overline{M} \rangle = \frac{\sum c_n \overline{M}_n}{\sum c_n} \quad (6)$$

$$\overline{M}_n = \sum_i f_{i,n} M_{i,n}. \quad (7)$$

252 where the index n refers to the the n^{th} atom of
253 the chemical formula, the index i refers to isotope
254 i of atom n , $M_{i,n}$ refers to the atomic mass of the
255 i^{th} isotope of atom n , \overline{M}_n is the average isotopic
256 mass of atom n , and $f_i(n)$ refers to the fractional
257 abundance of the i^{th} isotope of atom n .⁴ In the

same way, the average mass variance is

$$\langle \overline{\Delta M^2} \rangle = \frac{\sum c_n \overline{\Delta M_n^2}}{\sum c_n} \quad (8)$$

$$\overline{\Delta M_n^2} = \sum_i f_{i,n} (M_{i,n} - \overline{M}_n)^2. \quad (9)$$

In this development, our use of the isotropic con-
259 tinuum approximation implies that Equation 3
260 represents an average scattering rate for all acous-
261 tic phonon polarizations. While we use this defi-
262 nition in this work, it is worth noting that other
263 interpretations of the mass defect coefficient have
264 also been used [42, 43].

Once the coefficient B is calculated, it can be
265 input into G4CMP to model isotopic scattering,
266 where it acts as the scattering rate coefficient for
267 all three phonon polarizations. We present the
268 results of this calculation of B for several materials
269 of interest in Section 3.2.

272 **2.3 Phonon Density of States (DOS)**

273 During both anharmonic downconversion pro-
274 cesses and isotopic scattering processes (discussed
275 in Section 2.2) G4CMP uses the phonon density of
276 states to determine the randomly-drawn polariza-
277 tions of phonons produced after downconversions
278 and scatters. The LDOS, STDOS, and FTDOS
279 parameters in Table 5 are the fractional densities
280 of states for longitudinal, slow transverse, and fast
281 transverse acoustic phonons, respectively, and sum
282 to unity.

283 The calculation of the DOS values for these
284 materials is performed in two steps: computation
285 of a 3D phonon dispersion relationship $\omega(\vec{k})$ for
286 a material using its lattice properties, and com-
287 putation of the DOS from the phonon dispersion
288 relationship. For GaAs, Si, LiF, CaF₂, Al₂O₃ and
289 CaWO₄ we use lattice information from the Mat-
290 erials Data Repository [44] to calculate the phonon
291 dispersion. The lattice force constants from Mat-
292 erials Data Repository are then used as an input
293 to Phonopy, a separate software used in the
294 calculation of three-dimensional phonon disper-
295 sion relationships [45, 46]. From these dispersion
296 curves, we compute the contribution of the DOS
297 per phonon branch λ at given frequency ω , defined
298 as

$$g_\lambda(\omega) = \frac{1}{N} \sum_i \delta(\omega - \omega_i). \quad (10)$$

299 Here, the sum is over all phonon frequencies ω_i
300 of this branch in the first Brillouin zone obtained
301 from the grid points, N is the number of grid
302 points in the first Brillouin zone. In practice, this
303 is computed in Phonopy using a finite mesh of
304 $\omega(\vec{k})$ values, with the delta function treated as a

⁴We note here that formally, the sum over i may be different for different atoms s in the unit cell.

Table 2: Expressions for the Lamé constants and third-order isotropic elastic coefficients, calculated for the two non-cubic space groups (for which such expressions could not be found in literature). The space groups for these two materials are included for completeness.

| Material | Space Group | Parameter | Expression |
|--------------------------------|--------------------|-----------|---|
| Al ₂ O ₃ | R̄3c | μ | $(2C_{11} - C_{12} - 2C_{13} + C_{33} + 6C_{44} + 3C_{66})/15$ |
| | | λ | $(2C_{11} + 4C_{12} + 8C_{13} - 4C_{44} + C_{33} - 2C_{66})/15$ |
| | | α | $(-17C_{111} + 30C_{112} + 33C_{113} + 78C_{123} - 57C_{133} - 156C_{144} + 84C_{155} - 17C_{222} + C_{333} - 12C_{344})/105$ |
| | | β | $(71C_{111} + 4C_{112} - 11C_{113} - 68C_{123} + 103C_{133} + 220C_{144} - 140C_{155} - 55C_{222} + 2C_{333} + 4C_{344})/210$ |
| | | γ | $(-34C_{111} - 24C_{112} + 3C_{113} + 30C_{123} - 51C_{133} - 144C_{144} + 126C_{155} + 92C_{222} + 2C_{333} + 18C_{344})/210$ |
| | | μ | $(2C_{11} - C_{12} - 2C_{13} + C_{33} + 6C_{44} + 3C_{66})/15$ |
| CaWO ₄ | I4 ₁ /a | λ | $(2C_{11} + 4C_{12} + 8C_{13} + C_{33} - 4C_{44} - 2C_{66})/15$ |
| | | α | $(2C_{111} + 18C_{112} + 42C_{113} + 48C_{123} - 6C_{133} - 60C_{144} - 12C_{155} - 12C_{166} + C_{333} - 12C_{344} - 30C_{366} + 12C_{456})/105$ |
| | | β | $(4C_{111} + 8C_{112} - 7C_{113} - 30C_{123} + 23C_{133} + 76C_{144} + 4C_{155} + 4C_{166} + 2C_{333} + 4C_{344} + 38C_{366} - 72C_{456})/210$ |
| | | γ | $(2C_{111} - 3C_{112} + 6C_{123} - 6C_{133} - 18C_{144} + 9C_{155} + 9C_{166} + C_{333} + 9C_{344} - 9C_{366} + 27C_{456})/105$ |

gaussian of finite width. From this expression we can obtain the fractional contribution at 1 THz for acoustic phonons, which is the fractional DOS input required by G4CMP. Moreover, calculating the total DOS we can obtain the maximum acoustic phonon energy and maximum optical phonon energy (Debye Energy), the latter of which is also an input to G4CMP.

2.4 Propagation along Caustics

The propagation of acoustic phonons in a crystal is governed by the Green-Christoffel equation:

$$\rho\omega^2\epsilon_i = C_{ijkl}k_j k_k \epsilon_l, \quad (11)$$

where ω is the phonon frequency, ϵ_μ is the phonon polarization (longitudinal, transverse fast and transverse slow), k is the phonon wavevector, ρ is the crystal's mass density, and C_{ijkl} is again the elastic constant tensor. This equation arises from considering plane monochromatic elastic wave solutions to the equations governing an elastically deformed medium.

Propagation direction is governed by the group velocity $\vec{v}_g = \vec{\nabla}_k \omega$. As a result of an arbitrary crystal's anisotropic elastic tensor C_{ijkl} , the group velocity of a phonon may not be parallel with the phonon's wavevector \vec{k} [47, 48]. An initially isotropic distribution of wavevector \vec{k} therefore in general gives a nonuniform distribution of group velocity. This leads to a phenomenon known as “phonon focusing” in a crystal, from which “caustic” patterns are formed (Figure 3). These have

been measured experimentally in several experimental setups for a variety of different materials [49, 50, 51].

To successfully characterize acoustic phonon propagation direction in a new material, one then only requires the second-order elastic tensor components C_{ijkl} for the new material. These elastic tensor components used in this work are available for Al₂O₃ [52], GaAs [53], CaWO₄ [54], CaF₂ [31], and LiF [55]. For simulating phonon propagation in a new material, G4CMP only requires these second-order elastic tensor components. While in practice the caustic patterns emerging from crystal anisotropies are dependent on the energy of the phonon [53], G4CMP does not yet include this energy dependence and instead approximates this dependence as being weak in the limit of low phonon energy.

3 Model Results and Validation

In this section we demonstrate the above calculations as applied to Si, Ge, GaAs, Al₂O₃, LiF, CaWO₄, and CaF₂, and where possible use existing literature measurements to do a coarse validation of our calculations and the implementation into G4CMP. These are done for all four physical properties discussed in the subsections of Section 2: anharmonic downconversion, isotopic scattering, phonon density of states (DOS) and propagation along caustics.

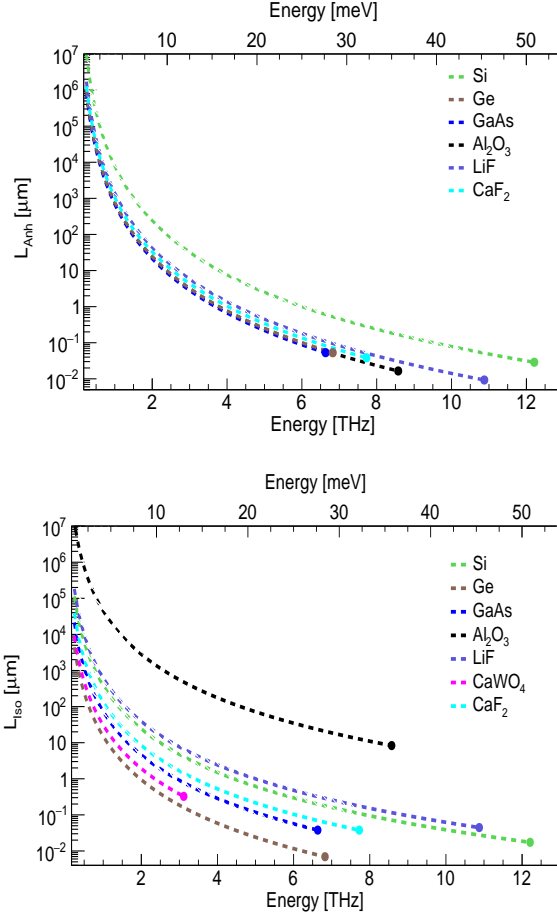


Figure 1: Characteristic length scales for anharmonic decay (top) and isotopic scattering (bottom) extracted from a cross-check simulation after implementing the calculated rates from Table 3. The dot points represents the maximum acoustic phonon energy ω_A extracted from table 5. For CaWO_4 's downconversion curve, the lower range of the literature-calculated downconversion coefficient $A_{c,l}$ is used.

3.1 Results: Anharmonic Downconversion

Table 3 presents our calculations of the second- and third-order isotropic elastic coefficients and the subsequent calculation of the parameter A in Equation 1. In these calculations, the second order elastic constants C_{ijkl} used in computing μ and λ as well as the third order elastic constants C_{ijklmn} used in computing α , β , and γ can be found in Appendix A. The calculations are done assuming phonon energies of 1 THz, which are within the “low-temperature” approximation assumed for Equation 1. We also present in Table 3 two additional values, $A_{c,l}$ and $A_{m,l}$, which are calculated values for A found in literature and experimentally measured values for A found in literature, respectively. In our calculations of A agree with literature calculations of $A_{c,l}$ to within a factor of few for most materials. There is some additional disagreement for sapphire, which we attribute to

two factors: the non-isotropy assumed in the calculations in Ref [56], and the steep fifth-power dependence on the assumed sound speed used to convert the results in Ref [56] into the form given in Equation 1. To the authors’ knowledge, only one of these materials has an $A_{m,l}$ that has been *measured* directly: CaF_2 . In Ref. [57], this parameter is measured using an optical technique that is sensitive to phonon absorption by a doublet of an Eu^{2+} dopant in the crystal that is tunable with applied stress. We leave additional discussion on experimental validation of this parameter for Section 4.

With these values calculated, we also integrate them into G4CMP and run a cross-check simulation to confirm the expected interaction rate. In this simulation, one million longitudinal acoustic phonons of varying energies are generated in a large block of material and allowed to propagate with isotopic scattering processes turned off. The block is large enough that surface interactions do not affect the phonon trajectories. For every longitudinal phonon generated, the distance from creation point to subsequent decay is tabulated and inserted into a histogram corresponding to that phonon’s energy. For each histogram, a characteristic decay length is tabulated, and that decay length appears as a function of energy in the top panel of Figure 1. In all materials tested, we find that the value of A derived from fits to these plots is consistent with the value of A used as input to G4CMP.

3.2 Results: Isotopic Scattering

Table 4 presents elements of the calculation for the isotopic scattering rate coefficient B found in Equation 3. Since in the isotropic continuum approximation the isotopic scattering rate simplifies to Equation 3, the main requirement is to calculate Γ_{md} for the material. For our calculations, we assume natural abundances of every atom within each material considered [62], which yields the values of Γ_{md} in the table. While isotopic enrichment of materials is possible, we present the rates from natural isotopic abundances to demonstrate a baseline strategy for how this calculation can be extended to other materials of interest for integration into G4CMP.

For isotopic scattering we again show our own calculation of B in Table 4 accompanied by literature calculations $B_{c,l}$ and literature measurements $B_{m,l}$ accompanied by references. Here, calculated scattering rates found in literature are generally found to be within a factor of a few of our estimates. Where there are measurements of this isotopic scattering rate, our estimates are similarly within a factor of a few of the measured literature values. Methods available in the literature

Table 3: Anharmonic downconversion parameters for a variety of target materials of interest. The calculated Lamé parameters (μ , λ) and third-order isotropic elastic coefficients (α , β , γ) are used to compute the anharmonic decay rate coefficient A found in Equation 1 and are included for completeness. For comparison we include calculated literature values $A_{c,l}$ and measured literature values $A_{m,l}$ for these materials where available. Values of $A_{c,l}$ do not always assume the same isotropic continuum approximation used in our calculation of A , and may quote a range of rates representing multiple propagation directions. $A_{m,l}$ was difficult to find in the literature for most materials here. We were also unable to find literature values for the third-order elastic constants of CaWO₄ for calculation of α , β , and γ , but nonetheless include CaWO₄ as other literature calculations of $A_{c,l}$ were found. For literature values $A_{c,l}$ and $A_{m,l}$, references are provided after the stated values.

| Material | μ [GPa] | λ [GPa] | α [GPa] | β [GPa] | γ [GPa] | F_{TT} | A [10 ⁻⁵⁵ s ⁴] | $A_{c,l}$ [10 ⁻⁵⁵ s ⁴] | $A_{m,l}$ [10 ⁻⁵⁵ s ⁴] |
|--------------------------------|----------------|--------------------|-------------------|------------------|-------------------|----------|--|--|--|
| Si | 68.58 | 53.68 | -227.37 | -55.97 | -107.97 | 0.75 | 1.15 | 0.741 [33] | — |
| Ge | 56.6 | 33.6 | -179.3 | -60.5 | -82.1 | 0.72 | 6.8 | 16.5 [33] | — |
| GaAs | 44.2 | 47.2 | -170.11 | -54.71 | -67.51 | 0.77 | 7.77 | 7.7-13.5 [33] | — |
| Al ₂ O ₃ | 166.24 | 139.8 | 95.13 | -27.02 | -152.8 | 0.67 | 12.7 | 1.88 [56] | — |
| LiF | 51.51 | 30.72 | -84.74 | -83.94 | -87.54 | 0.68 | 5.5 | 5.14 [33] | — |
| CaF ₂ | 45.15 | 65.2 | -135.21 | -95.85 | -43.69 | 0.75 | 6.14 | 7.0-10.4 [32] | 9.3 [57] |
| CaWO ₄ | 40.78 | 57.94 | — | — | — | — | — | 7.9 [58]-140 [59] | — |

Table 4: Isotopic scattering rates for the set of target materials of interest. We also include some inputs to the calculation that gives those rates: the lattice cell volume Ω and the polarization-averaged cubed sound speed $\langle c^3 \rangle$, as well as our calculation of the mass defect coefficient Γ_{md} . Ranges in the $B_{m,l}$ column correspond to measurements of different phonon polarizations. For literature values $B_{c,l}$ and $B_{m,l}$, references are provided after the stated values.

| Material | Ω [A ³] | Γ_{md} | $\langle c^3 \rangle$ [10 ¹¹ m ³ /s ³] | B [10 ⁻⁴² s ³] | $B_{c,l}$ [10 ⁻⁴² s ³] | $B_{m,l}$ [10 ⁻⁴² s ³] |
|--------------------------------|-------------------------------|-----------------------|---|--|--|--|
| Si | 2.0 | 2.02×10 ⁻⁴ | 2.13 | 2.33 | 2.42 | 2.42-2.56 [60] |
| Ge | 2.26 | 5.88×10 ⁻⁴ | 0.46 | 35.4 | 36.7 [38] | — |
| GaAs | 2.38 | 9.16×10 ⁻⁵ | 0.479 | 7.22 | 7.38 [39] | 5.9-29.5 [60] |
| Al ₂ O ₃ | 0.5 | 1.25×10 ⁻⁵ | 3.06 | 0.025 | — | 0.04 [58] |
| LiF | 0.81 | 1.36×10 ⁻⁴ | 1.19 | 1.17 | 1.69 [33] | — |
| CaF ₂ | 1.4 | 1.83×10 ⁻⁴ | 0.84 | 4.83 | 9.13 [61] | 20.3 [61] |
| CaWO ₄ | 1.3 | 2.02×10 ⁻⁴ | 0.22 | 15.0 | 2.4 [58]-59 [59] | — |

have taken on three forms: thermal conductivity measurements in Ref. [61], a phonon backscattering technique used by Ref. [58], and a technique in which phonons are scattered around a slot cut into the chip under test as in Ref. [60]. While these measurements are more commonly available than measurements of the anharmonic decay coefficient A , they are nonetheless still difficult to find for all of the materials we study.

To test isotopic scattering's implementation into G4CMP we implement the same cross-check procedure as before, but with anharmonic decay turned off within G4CMP. The results are shown in the bottom panel of Figure 1. As the isotopic scattering rate is averaged over the multiple different polarizations, this represents an average characteristic length for all phonon polarizations. We again find that the characteristic decay lengths are consistent with the input rates used and a ν^4 dependence.

3.3 Results: Density of States

For each of the crystal structures we study in this work, we compute phonon dispersion curves for the various phonon branches, and use these to construct branch-specific density of states curves as a function of energy (Figure 2). Fractional density of states contributions are then computed for acoustic longitudinal, fast transverse, and slow transverse phonons at 1 THz, with the results shown in Table 5. These values are used as inputs to G4CMP.

3.4 Results: Propagation along Causics

To demonstrate successful implementation of the physical processes responsible for phonon propagation along caustics, we compare simulated caustic patterns against experimental heat-pulse caustic measurements. For each material, we create a simple G4CMP geometry consisting of a 2mm cube of substrate with its +z face acting

Table 5: Fractional density of states TF:TS:L at 1 THz, maximum acoustic phonon frequency ω_A , maximum acoustic optical phonon frequency ω_O , and experimental maximum optical frequency ω_{OE} . The theoretical values are obtained using phonopy [45]. The rightmost column provides references for the ω_{OE} column's values.

| Material | TS:TF:L | ω_A [THz] | ω_O [THz] | ω_{OE} [THz] | Refs. |
|-------------------------|-------------------------|---------------------|---------------------|------------------------|-------|
| Si | 0.521 : 0.406 : 0.071 | 12.14 | 15.28 | 15.5 | [63] |
| Ge | 0.535 : 0.366 : 0.097 | 6.63 | 9.02 | 9.02 | [63] |
| GaAs | 0.584 : 0.337 : 0.078 | 6.56 | 8.58 | 8.82 | [64] |
| Al_2O_3 | 0.511 : 0.351 : 0.137 | 8.41 | 26.29 | 26.35 | [65] |
| LiF | 0.5156 : 0.386 : 0.0983 | 10.73 | 18.19 | 19.7 | [66] |
| CaF_2 | 0.599 : 0.318 : 0.0819 | 7.55 | 13.65 | 13.67 | [67] |
| CaWO_4 | 0.475 : 0.408 : 0.115 | 2.72 | 25.94 | 26.07 | [68] |

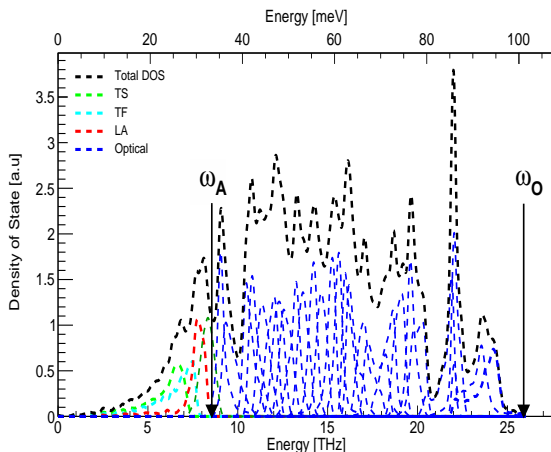


Figure 2: Phonon fractional density of states (DOS) for sapphire, showing the three acoustic branches (red, green, cyan) separately and showing all optical branches in the same color (blue). Black solid arrows are used to indicate the maximum acoustic ω_A and optical ω_O phonon frequencies.

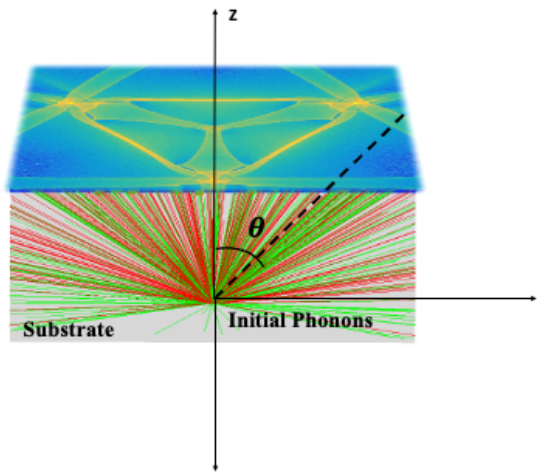


Figure 3: A rendering of the simulation to test G4CMP's propagation along caustics. The gray box is the substrate (sapphire, in this image), the red lines are transverse fast phonon trajectories, the green lines are transverse slow phonon trajectories, and θ is the angular scan range. The blue rectangle on the top surface of the substrate is the phonon collection plane, where brighter colors indicate more densely concentrated phonon impacts. Here, phonons were generated at the bottom of the substrate.

as a phonon collection plane (Figure 3). Anharmonic downconversion and isotopic scattering are turned off to have ballistic phonons. 40 million low-energy phonons (at 1 THz) are simulated isotropically from a point at $x = 0$, $y = 0$, and a z chosen to ensure that the collecting plane subtends the same angular scan range θ as those reported in experimental caustics probes. The locations of phonons landing on the collection plane are recorded, and histogrammed. The ratio of longitudinal to transverse-fast to transverse-slow polarizations used here is 0:1:1. This ratio is used primarily for comparison with the experimental data (see below), which often uses arrival-time-based gates to select the transverse phonon signal and cut away the longitudinal signal.⁵ The top panel

in Figure 4 (Figure 5) shows the resulting caustic patterns for sapphire, with the crystal direction $[1\bar{1}02]$ ($[0010]$) oriented out of the page. We also show simulated caustics for GaAs (Figure 6), LiF (Figure 7), CaWO_4 (Figure 8), and CaF_2 (Figure 9).

We validate our simulations against experimental caustics measurements from literature, shown in the bottom panels of Figures 4-9. Phonon caustics imaging has been achieved in a variety of materials, including all of the materials shown in Table 3. Such experiments typically proceed as follows. A crystal substrate under test is outfitted with a small, single bolometer (area $\simeq 50\mu\text{m} \times 50\mu\text{m}$) on one side and a metal film on the other, and is then cooled to cryogenic temperatures (few K scale or below). A phonon burst is then produced at cryogenic temperatures by pass-

⁵It is also worth noting that the longitudinal phonon signal commonly shows less pronounced caustic structures than transverse phonon signals in a variety of materials, often displaying only a central “hotspot” of detected phonons in such images.

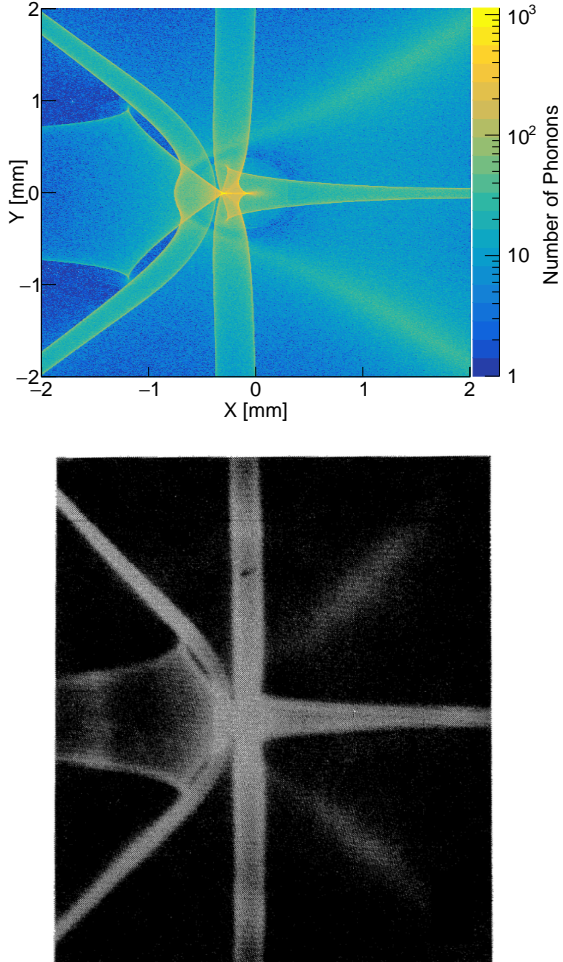


Figure 4: Top: phonon caustic image for sapphire (Al_2O_3) obtained from G4CMP. The crystal direction $[1\bar{1}02]$ is at the center of the pattern, oriented out-of-page. Bright regions indicate directions of high phonon flux. Bottom: phonon caustic image for sapphire measured at 1.6 K in Ref. [69], where the crystal direction $[1\bar{1}02]$ is out of page and horizontal scan range is $\pm 32^\circ$. This angular scan range matches that used in our simulations

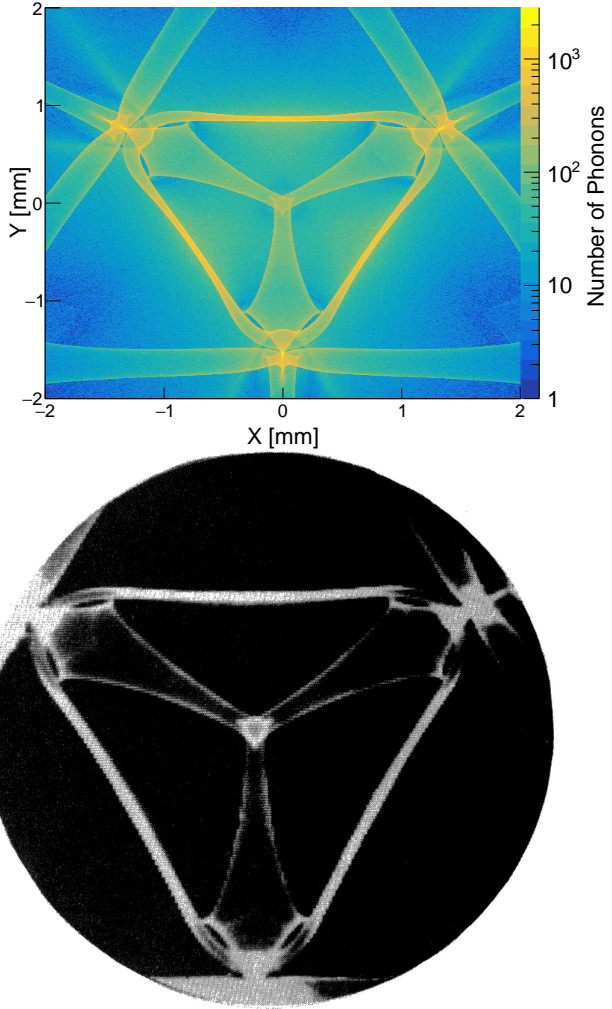


Figure 5: Top: phonon caustic image for sapphire (Al_2O_3) obtained from G4CMP. The crystal direction $[0010]$ is at the center of the pattern, oriented out-of-page. Bottom: phonon caustic image for sapphire measured at 1.6 K in Ref. [69], where the crystal direction $[0010]$ is out of page and horizontal scan range is $\pm 58^\circ$.

ing a short burst of current through the metal film or by illuminating the metal film locally with laser light. In this process, several non-spherical shells of longitudinal and transverse phonons are produced locally. Of these locally-created phonons, only those traveling in the direction of the bolometer are detected. While this experimental data-taking scheme is geometrically different from our simulation, functionally the mappings are identical: the pattern of phonons radiated from a point onto a surface (collecting plane) should be the same as the pattern of phonons radiated from an extended surface onto a point (bolometer). This enables comparisons between the simulated and experimentally-acquired images of these phonon caustics. In the comparisons we present, exact normalization of the different polarization components is not known for many of the experimen-

tal images, but in most⁶ cases the phonon images have been time-gated to select only transverse phonons. We therefore attempt to coarsely match this weighting of polarizations by using a 0:1:1 ratio for L:TF:TS phonons, but acknowledge that this may not yield a perfect match to the relative amplitudes of the measured caustic signals.

Even despite this uncertainty in the polarization weighting, the shapes of the resulting caustic images constructed with G4CMP and the shapes of the corresponding experimental images show strong agreement, implying successful integration of these new materials' phonon transport properties into G4CMP.

It is worth noting that many of the studies

⁶NB: Ref. [54] does not specify if these are time-gated to select only transverse phonons.

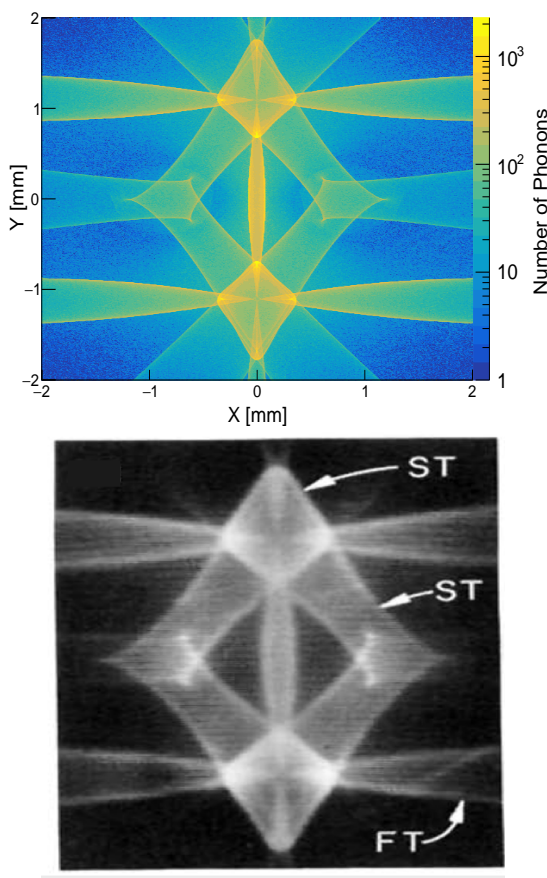


Figure 6: Top: phonon caustic image for GaAs obtained from G4CMP. The crystal direction [110] is at the center of the pattern, oriented out-of-page. Bottom: phonon caustic image for GaAs measured at 1.8 K in Ref. [70], where the crystal direction [110] is out of page and horizontal scan range is $\pm 59^\circ$.

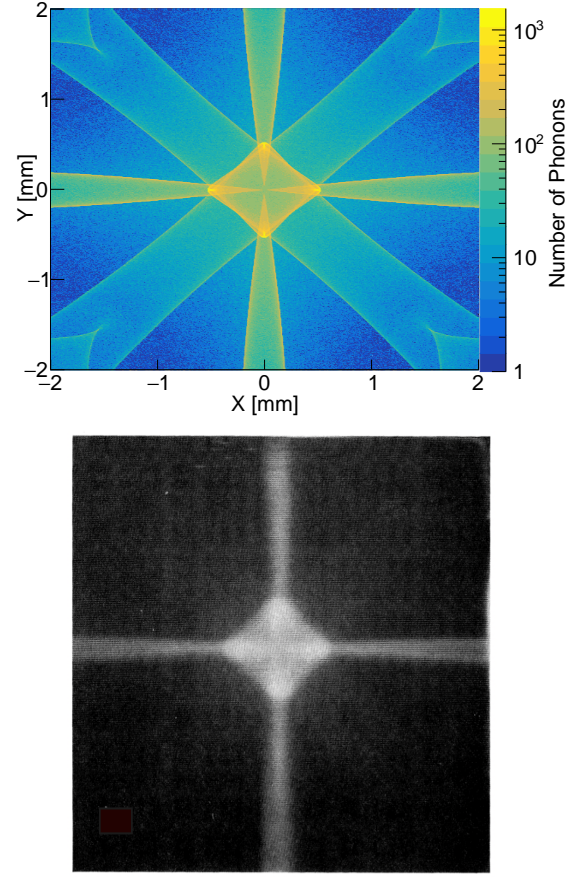


Figure 7: Top: phonon caustic image for LiF obtained from G4CMP. The crystal direction [100] is at the center of the pattern, oriented out-of-page. Bottom: phonon caustic image for LiF measured at 2.2 K in Ref. [71], where the crystal direction [100] is out of page and horizontal scan range is $\pm 40^\circ$.

from which we've obtained the experimental images also perform caustic simulations which show good agreement with their experimental results. However, to the authors' knowledge, these simulations have largely been done with separate custom simulation software dedicated to exploring caustics. This current work is not only a demonstration of a framework that we can use to reproduce similar results within a single public-facing software package, but also that we can do so within a package whose primary goal is an application of this physics to understanding low-energy detector response.

4 Discussion

The primary goal of this work has been to present and demonstrate a streamlined framework for integrating new materials into the G4CMP low-energy simulation software. The striking agreement between simulated and measured caustic diagrams for sapphire, LiF, GaAs, CaWO₄, and CaF₂

illustrate the general success of this implementation, and the relatively small set of required parameters needed for modeling this phonon transport within a publicly available software package. Moreover, the similar simplicity in input parameters for modeling anharmonic decay and isotopic scattering continues to paint an encouraging picture of accessibility for efforts to model phonon transport in future novel detector materials.

Given this modeling success, three natural topics of future interest are how one can further improve G4CMP's modeling capabilities, what work needs to be done to validate these models, and how this framework plays a role in particle detection and QIS applications.

From this work, we identify a few areas where future effort could be reasonably made to further improve realism in G4CMP's phonon modeling. First, the calculations here could be redone without using the isotropic continuum approximation in modeling downconversion and isotopic scattering. In G4CMP, the rates of these processes are ag-

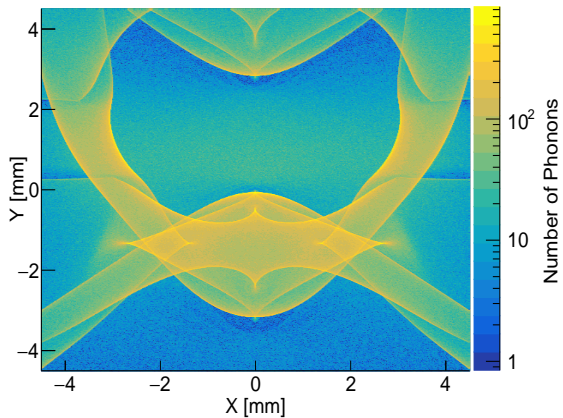


Figure 8: Top: phonon caustic image for CaWO_4 obtained from G4CMP. The crystal direction [010] is at the center of the pattern, oriented out-of-page. Bottom: phonon caustic image for CaWO_4 measured below 2 K in Ref. [54], where the crystal direction [010] is out of page and horizontal scan range is $\pm 56.3^\circ$.

In the simulation used to produce the top image, the crystal has been laterally extended to 9.1 mm square and 3 mm thick to enable a match to the scan range from the (bottom) experimental data.

589 nistic to the direction of the decaying/scattering
590 phonon. Ref. [32] demonstrates not only that the
591 rates of phonon downconversion vary by factors of
592 a few depending on the direction of propagation,
593 but also that in a rigorously-modeled anisotropic
594 scenario, more decay modes are possible than the
595 $L \rightarrow T + T$ and $L \rightarrow L + T$ that G4CMP cur-
596 rently models: both transverse fast and transverse
597 slow phonons may undergo anharmonic decay. As
598 G4CMP preserves the phonon direction and po-
599 larization information step-by-step, a natural ex-
600 tension of this work may therefore plausibly be
601 to implement this direction-dependence and more
602 complex polarization dependence of rate. Further-
603 more, while phonon scattering on isotropic impuri-
604 ties is handled as being isotropic in momentum
605 (k)-space according to G4CMP, this is not univer-
606 sally true: experiments in Ref [60] indicate that
607 there is also a degree of anisotropy to be expected

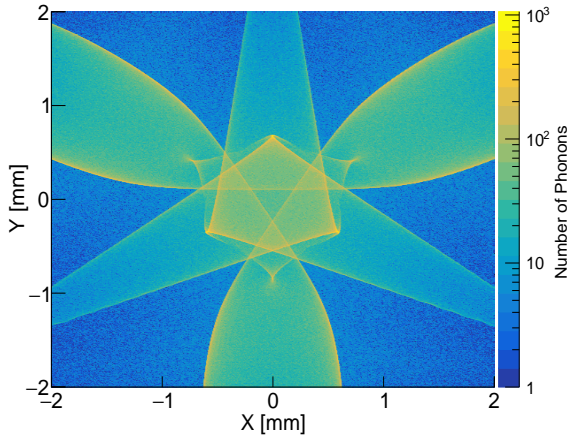


Figure 9: Top: phonon caustic image for CaF_2 obtained from G4CMP. The crystal direction [111] is at the center of the pattern, oriented out-of-page. Bottom: phonon caustic image for CaF_2 from Ref. [72], where the crystal direction [111] is out of page and horizontal scan range is $\pm 23^\circ$.

in the phonon scattering process, beyond that incurred from just propagation along caustics from the scattering site. Second, an improvement to G4CMP may include accounting for dispersion's impact on the phonon caustics, which currently do not (but should) change as a function of phonon energy [53]. This energy dependence may also be responsible for small degrees of disagreement observed between simulated and measured caustics patterns in Figures 4-9. Other improvements to G4CMP include modeling electron/hole transport and processes in these newly-added materials, adding photon interactions with the substrate, and developing functionality for quanta to traverse boundaries between different crystals (such as the interface between a substrate and its superconducting film). While a thorough discussion of these efforts is beyond the scope of this work, they will be the topic of follow-up studies.

The next critical insight from this work is that measured values of the downconversion and iso-
topic scattering rate coefficients, $A_{m,l}$ and $B_{m,l}$
(Tables 3 and 4) are not trivial to find for an arbit-

trary material, suggesting that experimental validation of phonon transport parameters is challenging. This is particularly true for anharmonic decay, in which we were only able to find one direct measurement $A_{m,l}$ for CaF_2 . This direct measurement relies on doping a crystal with Eu^{2+} atoms and taking advantage of the stress-dependence of optical transitions in that atom. Employing this strategy in an arbitrary material clearly runs into prohibitive challenges when the material bandgap is lower than the energy of the optical transitions accessible. While this strategy may be viable for directly measuring anharmonic decay rates in other optically clear materials, further study is needed to determine how broadly applicable it may be to arbitrary doped materials. Another possible (albeit less direct) means of measuring this may follow the heat-pulse strategy employed in Ref. [58]. Here, heat pulse transmission measurements are taken at cryogenic temperatures using a bolometer, and for sufficiently large heater powers, they are (plausibly) affected by anharmonic downconversion in the material. While such measurements are also affected by isotopic scattering and would have to simultaneously fit for both A and B , they nonetheless may grant some sensitivity to directly measuring downconversion rates. Measurements of the isotopic scattering are more straightforward to pursue, and may follow any of the prescriptions cited in Table 4. We believe the incompleteness in the $B_{m,l}$ column is likely to be due not to technical challenges with designing measurement, but insufficient community attention to measuring those materials in particular. Overall, we believe that the general lack of measured A and B values in the literature motivates the development of a dedicated test platform for measuring phonon propagation in various materials of interest and performing fits to validate the expansion of G4CMP’s phonon modeling to other novel materials.

Lastly, it is worth discussing how the tools developed here strengthen particle detection and QIS applications. While we used this framework to model several new materials, it can be readily extended in kind to arbitrary solid-state materials that are well-motivated from low-threshold sensing and QIS standpoints. Diamond, SiO_2 and AlN are particularly well-motivated dark matter targets as they are advantageous for looking for single-phonon excitations produced from a DM interaction through a hadrophilic scalar mediator [73]. Other more complex crystals with low electronic bandgaps such as $\text{Eu}_5\text{In}_2\text{Sb}_6$ are also of current interest for their lowered threshold (relative to Si and Ge) for charge readout [74]. If those are also used in an NTL phonon-amplification and sensing scheme, being able to understand phonon

propagation within them will also be critical for detector response modeling. From a QIS perspective, Si and Al_2O_3 are the most common substrates used, and are now both modeled in G4CMP. However, superconductors such as aluminum, niobium, and tantalum are all commonly used in ground plane and circuit design. Coupling this framework (applied to those materials) with an expansion of G4CMP’s ability to transport phonons between different crystals will enable rigorous characterization of microphysics in the superconducting layer, which is important for modeling quasiparticle-induced qubit errors. Though it is beyond the scope to discuss and analyze all well-motivated materials candidates for sensing and QIS, the framework presented here will enable more efficient modeling of these materials in G4CMP.

The results of this work may provide additional use in applications where particle impacts are expected to be spatially localized within a device. In such a scenario, these phonon models (and notably caustic patterns) may enable one to place sensors to maximize the chances of observing the emergent phonon pulses created from the impact point [26]. As more materials’ phonon transport properties are integrated into G4CMP, such strategies may be more easily used to improve a device’s detection efficiency. Overall, this framework’s general assistance in understanding a material’s microphysical phonon response provides the foundation for modeling signal and background responses in a dark matter direct detection experiment and for modeling phonon-induced correlated errors in superconducting qubits.

5 Conclusion

In this work, we have presented a condensed framework for adding phonon transport modeling into the G4CMP simulation package for new materials of interest to the dark matter direct detection and QIS communities. We have used this framework to explore phonon transport parameters needed by G4CMP for seven materials, five of which have not yet been integrated into a comprehensive low-energy simulation package: GaAs, Al_2O_3 , LiF, CaWO_4 , and CaF_2 . We have moreover accompanied this exploration with a literature search of calculated and measured phonon transport parameters for those materials, and find that the integration of our calculations into G4CMP gives phonon propagation that is largely consistent with calculated and/or measured decay rates, scattering rates, phonon density of states, and phonon caustics in those materials. As measurements for all materials were not found

744 in this search, it is also apparent that there is further room for experimental campaigns to help validate these phonon transport parameters for many
 745 materials of interest.
 746

748 6 Acknowledgements

749 The authors would like to thank Tanner Trickle
 750 for providing insights and suggesting strategies for
 751 calculating the density of states for various mate-
 752 rials. Finally, we thank the rest of the Fermilab
 753 QSC group for freeing up person-hours for the
 754 authors to develop this work. This manuscript has
 755 been authored by Fermi Research Alliance, LLC
 756 under Contract No. DE-AC02-07CH11359 with
 757 the U.S. Department of Energy, Office of Science,
 758 Office of High Energy Physics. This work was sup-
 759 ported by the U.S. Department of Energy, Office
 760 of Science, National Quantum Information Science
 761 Research Centers, Quantum Science Center and
 762 the U.S. Department of Energy, Office of Science,
 763 High-Energy Physics Program Office.

764 IH led the development of the work presented
 765 in this paper. RL and RK provided supporting
 766 checks to calculations in this work and shaped
 767 the narrative of the manuscript. RL, RK, and IH
 768 drafted the manuscript. EFF and LH provided
 769 regular feedback over the course of the included
 770 work. All authors helped in preparation of this
 771 paper on the presented result.

772 Appendix A Elastic Constants

773 In Table A.6 we provide numerical values of the
 774 elastic constants used in this work. The second-
 775 order elastic constants are used to model caustic
 776 propagation, and are also used to calculate the
 777 second-order parameters μ and λ needed for calcu-
 778 lation of the anharmonic decay coefficient A . The
 779 third-order elastic constants are used in finding α ,
 780 β , and γ , also needed for calculating the anhar-
 781 monic decay coefficient. All coefficients are given
 782 in (pressure) units of GPa. Sources for the elas-
 783 tic constants are found in the rightmost column.
 784 Standard third-order elastic constants for CaWO₄
 785 were not found.

786 Appendix B Density of States

787 We display phonon density of states curves for
 788 GaAs (Figure B.10), LiF (Figure B.11), and CaF₂
 789 (Figure B.12). These curves have significantly re-
 790 duced complexity in their optical branches relative
 791 to Al₂O₃ due to the smaller number of atoms in
 792 a unit cell. The Debye Frequency ω_O is used in
 793 G4CMP. The jitter in the DOS values at energies

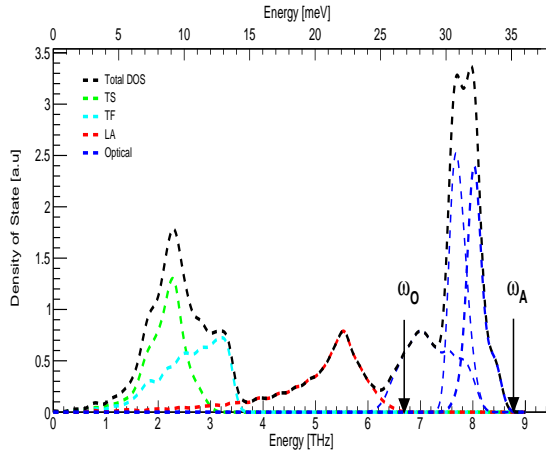


Figure B.10: Partial density of states of GaAs for transverse slow (green), transverse fast (cyan) and longitudinal (red) acoustic phonons. The blue curves to the right of the acoustic curves show the partial contribution of optical phonon channels to the DOS. The total density of states is the black line. ω_A corresponds to the maximum acoustic phonon energy and ω_O is the maximum optical phonon energy.

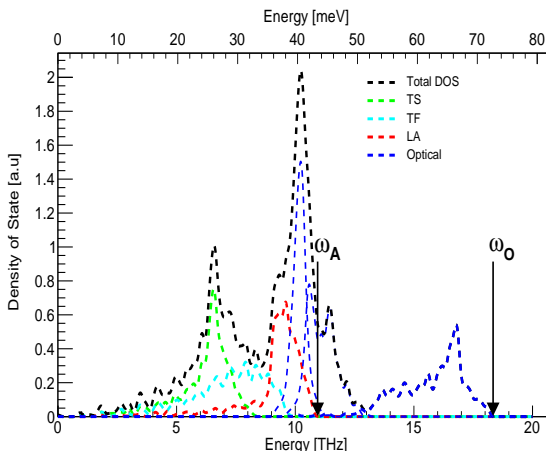


Figure B.11: Partial density of states of LiF for transverse slow (green), transverse fast (cyan) and longitudinal (red) acoustic phonons. The blue curves to the right of the acoustic curves show the partial contribution of optical phonon channels to the DOS. The total density of states is the black line. ω_A corresponds to the maximum acoustic phonon energy and ω_O is the maximum optical phonon energy.

below approximately 5 THz is due to low-statistics
 794 in the numbers of points computed during the
 795 dispersion calculation. However, for LDOS, FT DOS,
 796 and STDOS values in Table 5, a separate simula-
 797 tion with increased \vec{k} -space point density was used
 798 to avoid these fluctuations.
 799

800 References

- [1] A. Arbey, F. Mahmoudi, Dark matter and the early universe: A review, *Progress in Particle and Nuclear Physics* 119 (2021) 103865. doi:<https://doi.org/10.1016/j.ppnp.2021.103865>.

Table A.6: Values of the second and third-order elastic constants in GPa used on the calculation for anharmonic downconversion.

| Material | Second-order C ₁₁ ,C ₁₂ ,C ₄₄ [GPa] | Third-order C ₁₁₁ ,C ₁₁₂ ,C ₁₂₃ ,C ₁₄₄ ,C ₁₆₆ ,C ₄₅₆ [GPa] | Refs. |
|---|---|--|----------|
| Si | [167.8,65.2,80.1] | [-880,-515,27,74,-385,-40] | [31] |
| Ge | [126,44.67] | [-760,-410,-70,0,-310,-46] | [75] |
| GaAs | [121.1,57.4,59.5] | [-620,-392,-62.8,-274.3,-43] | [53] |
| CaF ₂ | [174.5,56.4,35.93] | [-1246,-400,-254,-124,-214,-75] | [76] |
| LiF | [111.2,42.0,62.8] | [-1646,-252,92,98,-261,97] | [77] |
| Second-order C ₁₁ ,C ₁₂ ,C ₁₃ ,C ₁₄ ,C ₃₄ ,C ₄₄ [GPa] | | Third-order C ₁₁₁ ,C ₁₁₂ ,C ₁₁₃ ,C ₁₁₄ ,C ₁₂₃ ,C ₁₂₄ ,C ₁₃₃ ,C ₁₃₄ , C ₁₄₄ ,C ₁₅₅ , C ₂₂₂ ,C ₃₃₃ ,C ₃₄₄ ,C ₄₄₄ [GPa] | |
| Al ₂ O ₃ | [495, 161.1, 111.1, -22.2, 499.9,-147.7] | [-394.6,-112.7,-91.9,8.1,-20.4,-5.5,-96.4,- 7.8,-38.2,-106.2,-453.4,-312.8,-113.1,4.1] | [52, 78] |
| Second-order C ₁₁ ,C ₁₂ ,C ₁₃ ,C ₁₆ ,C ₃₃ ,C ₄₄ ,C ₆₆ [GPa] | | Third-order C ₁₁₁ ,C ₁₁₂ ,C ₁₁₃ , C ₁₂₃ ,C ₁₃₃ ,C ₁₁₄ ,C ₁₅₅ ,C ₁₆₆ ,C ₃₃₃ , C ₃₄₄ ,C ₃₆₆ , C ₄₅₆ [GPa] | |
| CaWO ₄ | [151.5,65.6,45,18.8,134,35.4,40] | — | [79] |

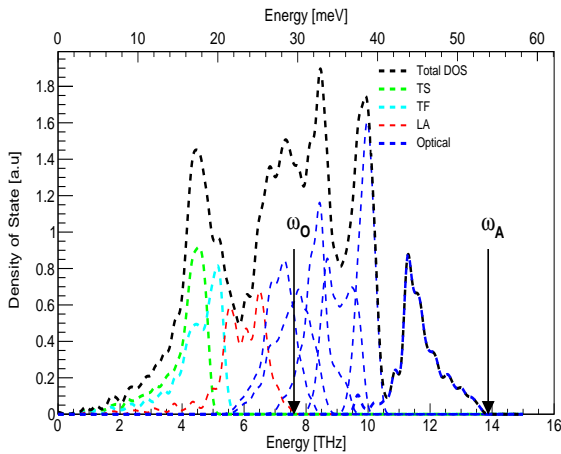


Figure B.12: Partial density of states of CaF₂ for transverse slow (green), transverse fast (cyan) and longitudinal (red) acoustic phonons. The blue curves to the right of the acoustic curves show the partial contribution of optical phonon channels to the DOS. The total density of states is the black line. ω_A corresponds to the maximum acoustic phonon energy and ω_O is the maximum optical phonon energy.

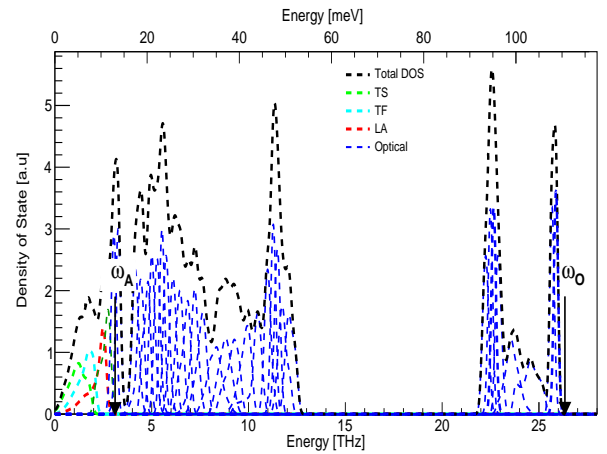


Figure B.13: Partial density of states of CaWO₄ for transverse slow (green), transverse fast (cyan) and longitudinal (red) acoustic phonons. The blue curves to the right of the acoustic curves show the partial contribution of optical phonon channels to the DOS. The total density of states is the black line. ω_A corresponds to the maximum acoustic phonon energy and ω_O is the maximum optical phonon energy.

- 805 URL <https://www.sciencedirect.com/science/article/pii/S0146641021000193> 821
806 [2] D. H. Weinberg, J. S. Bullock, F. Governato, 822
807 R. Kuzio de Naray, A. H. G. Peter, Cold dark matter: 823
808 Controversies on small scales, Proceedings of the 824
809 National Academy of Sciences 112 (40) (2015) 825
810 12249–12255. doi:10.1073/pnas.1308716112. 826
811 URL <http://dx.doi.org/10.1073/pnas.1308716112>
812 [3] N. Aghanim, et al., Planck2018 results: Vi. cosmological 827
813 parameters, Astronomy and Astrophysics 641 (2020) 828
814 A6. doi:10.1051/0004-6361/201833910. 829
815 URL <http://dx.doi.org/10.1051/0004-6361/201833910> 830
816 [4] J. Aalbers, et al., A search for new physics in low-energy 831
817 electron recoils from the first 1z exposure (2023). arXiv:2307.15753. 832
818 820

- [5] C. Bartram, et al., Search for invisible axion dark matter in the 3.3 – –4.2 μ eV mass range, Phys. Rev. Lett. 127 (2021) 261803. 823
URL <https://link.aps.org/doi/10.1103/PhysRevLett.127.261803> 824
[6] R. Essig, et al., Snowmass2021 Cosmic Frontier: The landscape of low-threshold dark matter direct detection in the next decade, arXiv e-prints (2022) arXiv:2203.08297arXiv:2203.08297, doi:10.48550/arXiv.2203.08297. 825
[7] C. W. Fink, S. L. Watkins, T. Aramaki, P. L. Brink, S. Ganjam, B. A. Hines, M. E. Huber, N. A. Kurinsky, R. Mahapatra, N. Mirabolfathi, W. A. Page, R. Partridge, M. Platt, M. Pyle, B. Sadoulet, B. Serfass, S. Zuber, Characterizing tes power noise for future 833
834 835 836

- single optical-phonon and infrared-photon detectors, AIP Advances 10 (8) (Aug. 2020). doi:10.1063/5.0011130.
[URL http://dx.doi.org/10.1063/5.0011130](http://dx.doi.org/10.1063/5.0011130)
- [8] D. J. Temples, et al., Performance of a kinetic inductance phonon-mediated detector at the nexus cryogenic facility (2024). arXiv:2402.04473.
- [9] R. Linehan, I. Hernandez, D. J. Temples, S. Q. Dang, D. Baxter, L. Hsu, E. Figueiroa-Feliciano, R. Khatiwada, K. Anyang, D. Bowring, G. Bratrud, G. Cancelo, A. Chou, R. Gaultieri, K. Stifter, S. Sussman, Estimating the energy threshold of phonon-mediated superconducting qubit detectors operated in an energy-relaxation sensing scheme (2024). arXiv:2404.04423.
- [10] C. W. Fink, C. P. Salemi, B. A. Young, D. I. Schuster, N. A. Kurinsky, The Superconducting Quasiparticle-Amplifying Transmon: A Qubit-Based Sensor for meV Scale Phonons and Single THz Photons (10 2023). arXiv:2310.01345.
- [11] P. N. Luke, Voltage-assisted calorimetric ionization detector, Journal of Applied Physics 64 (12) (1988) 6858–6860. arXiv:https://pubs.aip.org/aip/jap/article-pdf/64/12/6858/18621786/6858_1_online.pdf, doi:10.1063/1.341976.
[URL https://doi.org/10.1063/1.341976](https://doi.org/10.1063/1.341976)
- [12] B. S. Negayanov, V. N. Trofimov, Possibility of producing a bulky supersensitive thermal detector at a temperature close to absolute zero, 28 (1978) 356.
[URL http://jetpletters.ru/ps/0/article_24160.shtml](http://jetpletters.ru/ps/0/article_24160.shtml)
- [13] M. F. Albakry, et al., First measurement of the nuclear-recoil ionization yield in silicon at 100 ev, Phys. Rev. Lett. 131 (2023) 091801. doi:10.1103/PhysRevLett.131.091801.
[URL https://link.aps.org/doi/10.1103/PhysRevLett.131.091801](https://link.aps.org/doi/10.1103/PhysRevLett.131.091801)
- [14] M. F. Albakry, et al., Ionization yield measurement in a germanium cdmslite detector using photo-neutron sources, Phys. Rev. D 105 (2022) 122002. doi:10.1103/PhysRevD.105.122002.
[URL https://link.aps.org/doi/10.1103/PhysRevD.105.122002](https://link.aps.org/doi/10.1103/PhysRevD.105.122002)
- [15] R. Agnese, et al., Search for low-mass dark matter with cdmslite using a profile likelihood fit, Physical Review D 99 (6) (Mar. 2019). doi:10.1103/physrevd.99.062001.
[URL http://dx.doi.org/10.1103/PhysRevD.99.062001](http://dx.doi.org/10.1103/PhysRevD.99.062001)
- [16] R. Agnese, et al., Projected sensitivity of the supercdms snolab experiment, Physical Review D 95 (8) (Apr. 2017). doi:10.1103/physrevd.95.082002.
[URL http://dx.doi.org/10.1103/PhysRevD.95.082002](http://dx.doi.org/10.1103/PhysRevD.95.082002)
- [17] A. H. Abdelhameed, et al., First results from the cresst-iii low-mass dark matter program, Phys. Rev. D 100 (2019) 102002. doi:10.1103/PhysRevD.100.102002.
[URL https://link.aps.org/doi/10.1103/PhysRevD.100.102002](https://link.aps.org/doi/10.1103/PhysRevD.100.102002)
- [18] K. Ishidohiro, T. Kobayashi, K. Hosokawa, Y. Kawamura, Y. Kamei, S. Mima, C. Otani, A. A. Suzuki, M. Zulfakri, T. Taino, Kinetic inductance detectors on calcium fluoride substrate for astroparticle physics, Progress of Theoretical and Experimental Physics 2023 (10) (2023) 103H02. arXiv:<https://academic.oup.com/ptep/article-pdf/2023/10/103H02/52713177/ptad124.pdf>, doi:10.1093/ptep/ptad124.
[URL https://doi.org/10.1093/ptep/ptad124](https://doi.org/10.1093/ptep/ptad124)
- [19] S. Griffin, S. Knapen, T. Lin, K. M. Zurek, Directional detection of light dark matter with polar materials, Physical Review D 98 (11) (Dec. 2018). doi:10.1103/physrevd.98.115034.
[URL http://dx.doi.org/10.1103/PhysRevD.98.115034](http://dx.doi.org/10.1103/PhysRevD.98.115034)
- [20] S. Knapen, T. Lin, M. Pyle, K. M. Zurek, Detection of light dark matter with optical phonons in polar materials, Physics Letters B 785 (2018) 386–390. doi:10.1016/j.physletb.2018.08.064.
[URL http://dx.doi.org/10.1016/j.physletb.2018.08.064](http://dx.doi.org/10.1016/j.physletb.2018.08.064)
- [21] A. P. Read, B. J. Chapman, C. U. Lei, J. C. Curtis, S. Ganjam, L. Kratzzman, L. Frunzio, R. J. Schoelkopf, Precision measurement of the microwave dielectric loss of sapphire in the quantum regime with parts-per-billion sensitivity, Phys. Rev. Appl. 19 (2023) 034064. doi:10.1103/PhysRevApplied.19.034064.
[URL https://link.aps.org/doi/10.1103/PhysRevApplied.19.034064](https://link.aps.org/doi/10.1103/PhysRevApplied.19.034064)
- [22] J. M. Martinis, Saving superconducting quantum processors from decay and correlated errors generated by gamma and cosmic rays, npj Quantum Information 7 (1) (2021) 90. doi:10.1038/s41534-021-00431-0.
[URL https://doi.org/10.1038/s41534-021-00431-0](https://doi.org/10.1038/s41534-021-00431-0)
- [23] A. Bargerbos, L. J. Splitthoff, M. Pita-Vidal, J. J. Wesdorp, Y. Liu, P. Krogstrup, L. P. Kouwenhoven, C. K. Andersen, L. Grünhaupt, Mitigation of quasi-particle loss in superconducting qubits by phonon scattering, Phys. Rev. Appl. 19 (2023) 024014. doi:10.1103/PhysRevApplied.19.024014.
[URL https://link.aps.org/doi/10.1103/PhysRevApplied.19.024014](https://link.aps.org/doi/10.1103/PhysRevApplied.19.024014)
- [24] M. McEwen, et al., Resisting high-energy impact events through gap engineering in superconducting qubit arrays (2024). arXiv:2402.15644.
- [25] V. Iaia, et al., Phonon downconversion to suppress correlated errors in superconducting qubits., Nat Commun. 13 (6425) (2022). doi:<https://doi.org/10.1038/s41467-022-33997-0>.
- [26] M. Kelsey, et al., G4cmp: Condensed matter physics simulation using the geant4 toolkit, Nuclear Instruments and Methods in Physics Research Section A: Accelerators, Spectrometers, Detectors and Associated Equipment 1055 (2023) 168473. doi:10.1016/j.nima.2023.168473.
[URL http://dx.doi.org/10.1016/j.nima.2023.168473](http://dx.doi.org/10.1016/j.nima.2023.168473)
- [27] S. Barman, G. P. Srivastava, Long-wavelength nonequilibrium optical phonon dynamics in cubic and hexagonal semiconductors, Phys. Rev. B 69 (2004) 235208. doi:10.1103/PhysRevB.69.235208.
[URL https://link.aps.org/doi/10.1103/PhysRevB.69.235208](https://link.aps.org/doi/10.1103/PhysRevB.69.235208)
- [28] T. F. Harrelson, I. Hajar, O. A. Ashour, S. M. Griffin, Theoretical investigation of decoherence channels in athermal phonon sensors (2023). arXiv:2109.10988.
- [29] G. Srivastava, The Physics of Phonons, Taylor & Francis, 1990.
[URL https://books.google.com/books?id=OE-bHd2gzVgC](https://books.google.com/books?id=OE-bHd2gzVgC)
- [30] M. T. Labrot, A. P. Mayer, R. K. Wehner, P. E. Obermayer, Decay cascades of acoustic phonons in calcium fluoride, Journal of Physics: Condensed Matter 1 (45) (1989) 8809. doi:10.1088/0953-8984/1/45/006.
[URL https://dx.doi.org/10.1088/0953-8984/1/45/006](https://dx.doi.org/10.1088/0953-8984/1/45/006)
- [31] A. Berke, A. Mayer, R. Wehner, Spontaneous decay of acoustic phonons in calcium fluoride and silicon, Solid State Communications 54 (5) (1985) 395–397. doi:[https://doi.org/10.1016/0038-1098\(85\)90933-0](https://doi.org/10.1016/0038-1098(85)90933-0).
[URL https://www.sciencedirect.com/science/article/pii/0038109885909330](https://www.sciencedirect.com/science/article/pii/0038109885909330)
- [32] A. Berke, A. P. Mayer, R. K. Wehner, Spontaneous decay of long-wavelength acoustic phonons, Journal of Physics C: Solid State Physics 21 (12) (1988) 2305. doi:10.1088/0022-3719/21/12/014.
[URL http://dx.doi.org/10.1088/0022-3719/21/12/014](http://dx.doi.org/10.1088/0022-3719/21/12/014)

- 983 URL [https://dx.doi.org/10.1088/0022-3719/21/
984 12/014](https://dx.doi.org/10.1088/0022-3719/21/12/014)
- 985 [33] S.-i. Tamura, Spontaneous decay rates of la phonons
986 in quasi-isotropic solids, Phys. Rev. B 31 (1985) 2574–
987 2577. doi:[10.1103/PhysRevB.31.2574](https://doi.org/10.1103/PhysRevB.31.2574).
988 URL [https://link.aps.org/doi/10.1103/PhysRevB.
989 31.2574](https://link.aps.org/doi/10.1103/PhysRevB.31.2574)
- 990 [34] F. I. Fedorov, General Theory of Elastic Waves in
991 Crystals Based on Comparison with an Isotropic
992 Medium, Springer US, Boston, MA, 1968, pp. 169–
993 209. doi:[10.1007/978-1-4757-1275-9_5](https://doi.org/10.1007/978-1-4757-1275-9_5).
994 URL [https://doi.org/10.1007/
995 978-1-4757-1275-9_5](https://doi.org/10.1007/978-1-4757-1275-9_5)
- 996 [35] R. F. S. Hearmon, ‘Third-order’ elastic coefficients,
997 Acta Crystallographica 6 (4) (1953) 331–340. doi:
998 [10.1107/S0365110X53000909](https://doi.org/10.1107/S0365110X53000909).
999 URL [https://doi.org/10.1107/
1000 S0365110X53000909](https://doi.org/10.1107/S0365110X53000909)
- 1001 [36] B. Campbell-Deem, P. Cox, S. Knapen, T. Lin,
1002 T. Melia, Multiphonon excitations from dark matter
1003 scattering in crystals, Physical Review D 101 (3)
1004 (Feb. 2020). doi:[10.1103/physrevd.101.036006](https://doi.org/10.1103/physrevd.101.036006).
1005 URL [https://dx.doi.org/10.1103/PhysRevD.101.
1006 036006](https://dx.doi.org/10.1103/PhysRevD.101.036006)
- 1007 [37] Y. Itin, F. W. Hehl, The constitutive tensor of linear
1008 elasticity: Its decompositions, cauchy relations, null
1009 lagrangians, and wave propagation, Journal of Mathematical
1010 Physics 54 (4) (Apr. 2013). doi:[10.1063/1.4801859](https://doi.org/10.1063/1.4801859).
1011 URL <http://dx.doi.org/10.1063/1.4801859>
- 1012 [38] S.-i. Tamura, Isotope scattering of dispersive phonons
1013 in ge, Phys. Rev. B 27 (1983) 858–866. doi:[10.1103/PhysRevB.27.858](https://doi.org/10.1103/PhysRevB.27.858).
1014 URL [https://link.aps.org/doi/10.1103/PhysRevB.
1015 27.858](https://link.aps.org/doi/10.1103/PhysRevB.27.858)
- 1016 [39] S.-i. Tamura, Isotope scattering of large-wave-vector
1017 phonons in gaas and insb: Deformation-dipole and
1018 overlap-shell models, Phys. Rev. B 30 (1984) 849–854.
1019 doi:[10.1103/PhysRevB.30.849](https://doi.org/10.1103/PhysRevB.30.849).
1020 URL [https://link.aps.org/doi/10.1103/PhysRevB.
1021 30.849](https://link.aps.org/doi/10.1103/PhysRevB.30.849)
- 1022 [40] R. Gurunathan, R. Hanus, G. Snyder, Alloy scattering
1023 of phonons, Materials Horizons 7 (6) (2020) 1452–
1024 1456, publisher Copyright: © 2020 The Royal Society
1025 of Chemistry. doi:[10.1039/c9mh01990a](https://doi.org/10.1039/c9mh01990a).
- 1026 [41] D. T. Morelli, J. P. Heremans, G. A. Slack, Estimation
1027 of the isotope effect on the lattice thermal conductivity
1028 of group iv and group iii-v semiconductors, Phys.
1029 Rev. B 66 (2002) 195304. doi:[10.1103/PhysRevB.66.
1030 195304](https://doi.org/10.1103/PhysRevB.66.195304).
1031 URL [https://link.aps.org/doi/10.1103/PhysRevB.
1032 66.195304](https://link.aps.org/doi/10.1103/PhysRevB.66.195304)
- 1033 [42] R. Hanus, R. Gurunathan, L. Lindsay, M. T. Agne,
1034 J. Shi, S. Graham, G. Jeffrey Snyder, Thermal transport
1035 in defective and disordered materials, Applied
1036 Physics Reviews 8 (3) (2021) 031311. arXiv:[https://pubs.aip.org/aip/apr/article-pdf/doi/10.
1037 1063/5.0055593/19741856/031311\1_online.pdf](https://pubs.aip.org/aip/apr/article-pdf/doi/10.1063/5.0055593/19741856/031311\1_online.pdf),
1038 doi:[10.1063/5.0055593](https://doi.org/10.1063/5.0055593).
1039 URL <https://doi.org/10.1063/5.0055593>
- 1040 [43] N. H. Protik, C. Draxl, Beyond the tamura model of
1041 phonon-isotope scattering, Phys. Rev. B 109 (2024)
1042 165201. doi:[10.1103/PhysRevB.109.165201](https://doi.org/10.1103/PhysRevB.109.165201).
1043 URL [https://link.aps.org/doi/10.1103/PhysRevB.
1044 109.165201](https://link.aps.org/doi/10.1103/PhysRevB.109.165201)
- 1045 [44] A. Jain, S. P. Ong, G. Hautier, W. Chen, W. D.
1046 Richards, S. Dacek, S. Cholia, D. Gunter, D. Skinner,
1047 G. Ceder, K. A. Persson, Commentary: The Materials Project: A materials genome approach to accelerating materials innovation, APL Materials 1 (1) (2013) 011002. arXiv:[https://pubs.aip.org/aip/apm/article-pdf/doi/10.
1048 1063/1.4812323/13163869/011002\1_online.pdf](https://pubs.aip.org/aip/apm/article-pdf/doi/10.1063/1.4812323/13163869/011002\1_online.pdf),
1049 doi:[10.1063/1.4812323](https://doi.org/10.1063/1.4812323).
- 1050 URL <https://doi.org/10.1063/1.4812323>
- 1051 [45] A. Togo, L. Chaput, T. Tadano, I. Tanaka, Implementation
1052 strategies in phonopy and phono3py, J. Phys. Condens. Matter 35 (35) (2023) 353001. doi:
1053 [10.1088/1361-648X/acd831](https://doi.org/10.1088/1361-648X/acd831).
1054 URL <https://doi.org/10.1063/1.4812323>
- 1055 [46] A. Togo, First-principles phonon calculations with
1056 phonopy and phono3py, J. Phys. Soc. Jpn. 92 (1)
1057 (2023) 012001. doi:[10.7566/JPSJ.92.012001](https://doi.org/10.7566/JPSJ.92.012001).
1058 URL [https://link.aps.org/doi/10.1103/
1059 PhysRevLett.43.1424](https://link.aps.org/doi/10.1103/PhysRevLett.43.1424)
- 1060 [47] F. Rösch, O. Weis, Geometric propagation of acoustic
1061 phonons in monocrystals within anisotropic continuum
1062 acoustics, Zeitschrift fur Physik B Condensed Matter 25 (2) (1976) 101–114. doi:[10.1007/
1063 BF01320167](https://doi.org/10.1007/BF01320167).
1064 URL [https://doi.org/10.1007/
1065 BF01320167](https://doi.org/10.1007/BF01320167)
- 1066 [48] S. Leman, Review article: Physics and monte carlo
1067 techniques as relevant to cryogenic, phonon and ionization
1068 readout of cdms radiation-detectors (09 2011).
1069 URL [https://doi.org/10.1007/
1070 BF01320167](https://doi.org/10.1007/BF01320167)
- 1071 [49] G. A. Northrop, J. P. Wolfe, Ballistic phonon
1072 imaging in solids—a new look at phonon focusing,
1073 Phys. Rev. Lett. 43 (1979) 1424–1427.
1074 doi:[10.1103/PhysRevLett.43.1424](https://doi.org/10.1103/PhysRevLett.43.1424).
1075 URL [https://link.aps.org/doi/10.1103/
1076 PhysRevLett.43.1424](https://link.aps.org/doi/10.1103/PhysRevLett.43.1424)
- 1077 [50] J. P. Wolfe, Imaging Phonons: Acoustic Wave Propagation
1078 in Solids, Cambridge University Press, 1998.
- 1079 [51] K. Jakata, A. Every, Frequency dependence of
1080 dispersive phonon images : research article, South
1081 African Journal of Science 104 (9) (2008) 374–378.
1082 arXiv:[https://journals.co.za/doi/pdf/10.10520/
1083 EJC96837](https://journals.co.za/doi/pdf/10.10520/EJC96837), doi:[10.10520/EJC96837](https://doi.org/10.10520/EJC96837).
1084 URL [https://journals.co.za/doi/abs/10.10520/
1085 EJC96837](https://journals.co.za/doi/abs/10.10520/EJC96837)
- 1086 [52] A. G. Every, G. L. Koos, J. P. Wolfe, Ballistic phonon
1087 imaging in sapphire: Bulk focusing and critical-cone
1088 channeling effects, Phys. Rev. B 29 (1984) 2190–2209.
1089 doi:[10.1103/PhysRevB.29.2190](https://doi.org/10.1103/PhysRevB.29.2190).
1090 URL [https://link.aps.org/doi/10.1103/PhysRevB.
1091 29.2190](https://link.aps.org/doi/10.1103/PhysRevB.29.2190)
- 1092 [53] S.-i. Tamura, T. Harada, Focusing of large-wave-vector
1093 phonons in gaas, Phys. Rev. B 32 (1985) 5245–5250.
1094 doi:[10.1103/PhysRevB.32.5245](https://doi.org/10.1103/PhysRevB.32.5245).
1095 URL [https://link.aps.org/doi/10.1103/PhysRevB.
1096 32.5245](https://link.aps.org/doi/10.1103/PhysRevB.32.5245)
- 1097 [54] M. Msall, T. Head, D. Jumper, Low-temperature
1098 group velocity and elasticity in cawo4, Solid
1099 State Communications 150 (27) (2010) 1192–1195.
1100 doi:<https://doi.org/10.1016/j.ssc.2010.04.014>.
1101 URL [https://www.sciencedirect.com/science/
1102 article/pii/S0038109810002292](https://www.sciencedirect.com/science/article/pii/S0038109810002292)
- 1103 [55] C. V. Briscoe, C. F. Squire, Elastic constants of lif
1104 from 4.2°k to 300°k by ultrasonic methods, Phys. Rev.
1105 106 (1957) 1175–1177. doi:[10.1103/PhysRev.106.
1106 1175](https://doi.org/10.1103/PhysRev.106.1175).
1107 URL <https://doi.org/10.1103/PhysRev.106.1175>
- 1108 [56] H. J. Maris, S. Tamura, Propagation of acoustic
1109 phonon solitons in nonmetallic crystals, Phys. Rev. B
1110 84 (2011) 024301. doi:[10.1103/PhysRevB.84.024301](https://doi.org/10.1103/PhysRevB.84.024301).
1111 URL [https://link.aps.org/doi/10.1103/PhysRevB.
1112 84.024301](https://link.aps.org/doi/10.1103/PhysRevB.84.024301)
- 1113 [57] R. Baumgartner, M. Engelhardt, K. F. Renk, Spon-
1114 taneous decay of high-frequency acoustic phonons
1115 in caf₂, Phys. Rev. Lett. 47 (1981) 1403–1407.
1116 doi:[10.1103/PhysRevLett.47.1403](https://doi.org/10.1103/PhysRevLett.47.1403).
1117 URL [https://doi.org/10.1103/PhysRevLett.
1118 47.1403](https://doi.org/10.1103/PhysRevLett.47.1403)
- 1119 [58] J. Wigmore, A. Kozorezov, H. bin Rani, M. Giltrow,
1120 H. Kraus, B. Taele, Scattering of thz phonons, Phys-
1121 ica B: Condensed Matter 316–317 (2002) 589–591,
1122 proceedings of the 10th International Conference on
1123 Phonon Scatte ring in Condensed Matter. doi:[https://doi.org/10.1016/
1124 S0921-4526\(02\)00581-1](https://doi.org/10.1016/S0921-4526(02)00581-1).
1125 URL [https://www.sciencedirect.com/science/
1126 article/pii/S0921452602005811](https://www.sciencedirect.com/science/article/pii/S0921452602005811)
- 1127 URL [https://doi.org/10.1016/
1128 S0921-4526\(02\)00581-1](https://doi.org/10.1016/S0921-4526(02)00581-1)

- [59] K. Hayasaka, R. Higashi, J. Suda, Y. Tanaka, S. Tamura, M. Giltrow, J. Wigmore, Anomalous mode, elastic constants and phonon images in cawo4, Solid State Communications 143 (8) (2007) 386–389. doi:<https://doi.org/10.1016/j.ssc.2007.06.018>. URL <https://www.sciencedirect.com/science/article/pii/S0038109807004589>
- [60] S. Tamura, J. Shields, M. Ramsbey, J. Wolfe, Measurements of phonon elastic scattering rates by phonon imaging and monte-carlo simulation, in: Phonon Scattering in Condensed Matter VII: Proceedings of the Seventh International Conference, Cornell University, Ithaca, New York, August 3–7, 1992, Springer, 1993, pp. 79–83.
- [61] J. A. Harrington, C. T. Walker, Phonon scattering by point defects in caf_2 , srf_2 , and baf_2 , Phys. Rev. B 1 (1970) 882–890. doi:<https://doi.org/10.1103/PhysRevB.1.882>. URL <https://link.aps.org/doi/10.1103/PhysRevB.1.882>
- [62] J. R. de Laeter, J. K. Böhlke, P. D. Bièvre, H. Hidaka, H. S. Peiser, K. J. R. Rosman, P. D. P. Taylor, Atomic weights of the elements. review 2000 (iupac technical report), Pure and Applied Chemistry 75 (6) (2003) 683–800 [cited 2024-06-05]. doi:<https://doi.org/10.1351/pac200375060683>
- [63] I. Richman, Longitudinal Optical Phonons in CaF_2 , SrF_2 , and BaF_2 , The Journal of Chemical Physics 41 (9) (1964) 2836–2837. arXiv: https://pubs.aip.org/aip/jcp/article-pdf/41/9/2836/18836140/2836_1__online.pdf, doi:<https://doi.org/10.1063/1.1726360>
- [64] D. von der Linde, J. Kuhl, H. Klingenberg, Raman scattering from nonequilibrium lo phonons with picosecond resolution, Phys. Rev. Lett. 44 (1980) 1505–1508. doi:<https://doi.org/10.1103/PhysRevLett.44.1505>. URL <https://link.aps.org/doi/10.1103/PhysRevLett.44.1505>
- [65] J. Shan, F. Wang, E. Knosel, M. Bonn, T. F. Heinz, Measurement of the frequency-dependent conductivity in sapphire, Phys. Rev. Lett. 90 (2003) 247401. doi:<https://doi.org/10.1103/PhysRevLett.90.247401>. URL <https://link.aps.org/doi/10.1103/PhysRevLett.90.247401>
- [66] H. J. Hou, H. Guan, S. R. Zhang, L. H. Xie, L. Wang, Structural, phonon and thermodynamic properties of the rocksalt structure lif from first principles, in: Methods of Design and Characterization of Materials, Research and Development of Technological Processes, Vol. 850 of Materials Science Forum, Trans Tech Publications Ltd, 2016, pp. 348–353. doi:<https://www.scientific.net/MSF.850.348>.
- [67] I. Richman, Longitudinal Optical Phonons in CaF_2 , SrF_2 , and BaF_2 , The Journal of Chemical Physics 41 (9) (1964) 2836–2837. arXiv: https://pubs.aip.org/aip/jcp/article-pdf/41/9/2836/18836140/2836_1__online.pdf, doi:<https://doi.org/10.1063/1.1726360>. URL <https://doi.org/10.1063/1.1726360>
- [68] J. Suda, T. Sato, Temperature dependence of the linewidth of the first-order raman spectra for cawo 4 crystal, Journal of the Physical Society of Japan 66 (6) (1997) 1707–1713. arXiv: <https://doi.org/10.1143/JPSJ.66.1707>. URL <https://doi.org/10.1143/JPSJ.66.1707>
- [69] A. G. Every, G. L. Koos, J. P. Wolfe, Ballistic phonon imaging in sapphire: Bulk focusing and critical-cone channeling effects, Phys. Rev. B 29 (1984) 2190–2209. doi:<https://doi.org/10.1103/PhysRevB.29.2190>. URL <https://link.aps.org/doi/10.1103/PhysRevB.29.2190>
- [70] G. A. Northrop, S. E. Hebboul, J. P. Wolfe, Lattice dynamics from phonon imaging, Phys. Rev. Lett. 55 (1985) 95–98. doi:<https://doi.org/10.1103/PhysRevLett.55.95>. URL <https://link.aps.org/doi/10.1103/PhysRevLett.55.95>
- [71] G. A. Northrop, E. J. Cotts, A. C. Anderson, J. P. Wolfe, Phonon imaging of highly dislocated lif, Phys. Rev. Lett. 49 (1982) 54–57. doi:<https://doi.org/10.1103/PhysRevLett.49.54>. URL <https://link.aps.org/doi/10.1103/PhysRevLett.49.54>
- [72] D. C. Hurley, J. P. Wolfe, Phonon focusing in cubic crystals, Phys. Rev. B 32 (1985) 2568–2587. doi:<https://doi.org/10.1103/PhysRevB.32.2568>. URL <https://link.aps.org/doi/10.1103/PhysRevB.32.2568>
- [73] S. M. Griffin, K. Inzani, T. Trickle, Z. Zhang, K. M. Zurek, Multichannel direct detection of light dark matter: Target comparison, Phys. Rev. D 101 (5) (2020) 055004. arXiv: [1910.10716](https://arxiv.org/abs/1910.10716), doi:<https://doi.org/10.1103/PhysRevD.101.055004>
- [74] S. Watkins, Searching for light dark matter with narrow-gap semiconductors: The splendor experiment, tAUP 2023 (2023).
- [75] R. C. Tripathi, G. S. Verma, Third-Order Elastic Constants of Ge at Room and Liquid-Nitrogen Temperatures, Journal of Applied Physics 41 (7) (1970) 2999–3002. arXiv: https://pubs.aip.org/aip/jap/article-pdf/41/7/2999/18354708/2999_1__online.pdf, doi:<https://doi.org/10.1063/1.1659352>. URL <https://doi.org/10.1063/1.1659352>
- [76] M. T. Labrot, A. P. Mayer, R. K. Wehner, P. E. Obermayer, Decay cascades of acoustic phonons in calcium fluoride, Journal of Physics: Condensed Matter 1 (45) (1989) 8809. doi:<https://doi.org/10.1088/0953-8984/1/45/006>. URL <https://dx.doi.org/10.1088/0953-8984/1/45/006>
- [77] S. Mori, Y. Hiki, Calculation of the third- and fourth-order elastic constants of alkali halide crystals, Journal of the Physical Society of Japan 45 (5) (1978) 1449–1456. arXiv: <https://doi.org/10.1143/JPSJ.45.1449>, doi:<https://doi.org/10.1143/JPSJ.45.1449>. URL <https://doi.org/10.1143/JPSJ.45.1449>
- [78] R. E. Hankey, D. E. Schuele, Third-Order Elastic Constants of Al_2O_3 , The Journal of the Acoustical Society of America 48 (1B) (2005) 190–202. arXiv: https://pubs.aip.org/asa/jasa/article-pdf/48/1B/190/11610699/190_1__online.pdf, doi:<https://doi.org/10.1121/1.1912116>. URL <https://doi.org/10.1121/1.1912116>
- [79] P. Blanchfield, A. Miller, G. Saunders, Acoustic symmetry and the third order elastic constants of tetragonal tii (4/m) crystals, Journal of Physics and Chemistry of Solids 44 (6) (1983) 569–577. doi: [https://doi.org/10.1016/0022-3697\(83\)90047-1](https://doi.org/10.1016/0022-3697(83)90047-1). URL <https://www.sciencedirect.com/science/article/pii/0022369783900471>